A scaling theory for the size distribution of emitted dust aerosols suggests climate models underestimate the size of the global dust cycle

Jasper F. Kok[1]

Advanced Study Program, National Center for Atmospheric Research, Boulder, CO 80307

Edited by Inez Y. Fung, University of California, Berkeley, CA, and approved October 27, 2010 (received for review October 4, 2010)

Mineral dust aerosols impact Earth's radiation budget through interactions with clouds, ecosystems, and radiation, which constitutes a substantial uncertainty in understanding past and predicting future climate changes. One of the causes of this large uncertainty is that the size distribution of emitted dust aerosols is poorly understood. The present study shows that regional and global circulation models (GCMs) overestimate the emitted fraction of clay aerosols (<2 μm diameter) by a factor of ~2–8 relative to measurements. This discrepancy is resolved by deriving a simple theoretical expression of the emitted dust size distribution that is in excellent agreement with measurements. This expression is based on the physics of the scale-invariant fragmentation of brittle materials, which is shown to be applicable to dust emission. Because clay aerosols produce a strong radiative cooling, the overestimation of the clay fraction causes GCMs to also overestimate the radiative cooling of a given quantity of emitted dust. On local and regional scales, this affects the magnitude and possibly the sign of the dust radiative forcing, with implications for numerical weather forecasting and regional climate predictions in dusty regions. On a global scale, the dust cycle in most GCMs is tuned to match radiative measurements, such that the overestimation of the radiative cooling of a given quantity of emitted dust has likely caused GCMs to underestimate the global dust emission rate. This implies that the deposition flux of dust and its fertilizing effects on ecosystems may be substantially larger than thought.

direct radiative forcing | scale invariance | aeolian saltation | dust storms | wind erosion

Mineral dust aerosols eroded from arid soils impact weather and climate by scattering and absorbing radiation (1–4) and by modifying cloud properties (1, 5). Deposition of dust aerosols also partially controls the productivity and carbon sequestration of ocean ecosystems by providing limiting micronutrients such as iron, which affects atmospheric concentrations of greenhouse gases (6). The total impact of dust aerosols on Earth's radiative budget constitutes an important uncertainty in understanding past and predicting future climate changes (1, 6–8). In addition, dust aerosols adversely affect human health (9) and could suppress hurricane activity (10).

All these processes depend on the size of the atmospheric dust aerosols (2–5), which also determines their lifetime (3). But current treatments of the particle size distribution (PSD) of emitted dust aerosols in global circulation models (GCMs) are based on empirical relations with limited or no physical basis (3, 11–13). This use of empirical relations is necessary both because of the scarcity of measurements (14, 15) and because the understanding of the physical processes that determine the emitted dust PSD is very limited (16, 17). As a consequence, the fraction of emitted dust aerosols in the clay size range (<2 μm diameter), which both interact most efficiently with shortwave (solar) radiation and have the longest lifetime, differs by up to a factor of 4 between GCMs (3, 11–13, 18–20).

The availability of an accurate expression for the emitted dust PSD could thus reduce the uncertainty on GCM estimates of dust climate forcing. The present study derives such an expression from the analogy between the fragmentation of soil dust aggregates and the much better understood fragmentation of brittle materials such as glass (21). The resulting theoretical expression for the emitted dust PSD is in excellent agreement with measurements. In contrast, GCMs overestimate the emitted fraction of clay aerosols by a factor of ~2–8, with implications for simulations of the spatial distribution, radiative forcing, and global emission rate of dust aerosols.

The Physics of Dust Emission

Dust aerosols that undergo long-range transport predominantly have diameters smaller than 20 μm (22) and are denoted here as PM20 dust. The cohesive forces on such small particles in soils are generally much larger than aerodynamic forces (22), thereby preventing PM20 dust from being lifted directly by wind (15, 22). Moreover, these strong cohesive forces cause PM20 dust to rarely occur loosely in soils because they easily attach to other particles, thereby forming dust aggregates of larger sizes (17, 23).

Instead of being lifted directly by wind, PM20 dust is generally emitted by an intermediary process called saltation (22, 24). In saltation, larger sand-sized particles [~70–500 μm (22)], which are more easily lifted by wind because their cohesive forces are small compared to aerodynamic forces (22), move in ballistic trajectories (24). Upon impact on the soil bed, these saltating particles can eject dust particles from dust aggregates in the soil (22), a process known as sandblasting (22, 23). In addition, some saltating particles are sand-sized aggregates of dust particles, which can fragment and emit dust aerosols upon striking the surface (17).

Although the processes leading to dust emission are qualitatively understood, a detailed quantitative understanding is hindered by the large, highly variable, and poorly understood cohesive forces on PM20 dust in soils (16, 17, 22). As a consequence, previous physically based theories of dust emission that account for cohesive forces (16, 17) have large uncertainties in their input parameters and can differ greatly from measurements (17). I therefore take a different approach here and utilize the closest analog problem to dust emission that is quantitatively understood: the fragmentation of brittle materials (21, 25).

The Fragmentation of Brittle Materials

When a brittle material such as glass or gypsum receives a large input of energy, for example by being dropped on a hard surface

Author contributions: J.F.K. designed research, performed research, analyzed data, and wrote the paper.

The author declares no conflict of interest.

This article is a PNAS Direct Submission.

[1]E-mail: jfkok@umich.edu.

This article contains supporting information online at www.pnas.org/lookup/suppl/doi:10.1073/pnas.1014798108/-/DCSupplemental.

(26), the resulting fragment PSD can be classified into three regimes (21, 27):

1. The elastic regime: for low energies, the brittle object remains intact and no fragments are produced.
2. The damage regime: for larger energies, the object breaks into two or more fragments, but the size of the largest fragment is comparable to the original size of the object.
3. The fragmentation regime: for even larger energies, the brittle object fragments into a wide range of particle sizes, for which the size of the largest fragment is small compared to that of the original object.

Measurements show that the PSD in the fragmentation regime follows a power law (21, 26, 28, 29) and is thus "scale invariant" (30) (Fig. 1). Specifically, measurements and theory show that the PSD arising from the fragmentation of spherical, brittle objects is well-described by (21, 28)

$$\frac{dN_f}{d\ln D_f} \propto D_f^{-2}, \qquad (x_0 < D_f < \lambda), \qquad [1]$$

where N_f is the number of fragments with size D_f. This power law is valid for fragments larger than the indivisible constituent size x_0 and smaller than the side crack propagation length λ, the physical significance of which are discussed below.

The reason for the occurrence of scale invariance in brittle material fragmentation is rooted in the mechanism by which fragments are created: through the propagation and merger of cracks. When a brittle object is stressed, for example, by a physical impact, such cracks can propagate along imperfections that locally weaken the material, such as microscopic cracks (21, 29, 31). If the stress is large enough, the material will fail at the tips of the microscopic cracks, causing a larger crack to propagate perpendicular to the stress direction, much like ripping a tear in a piece of fabric. As a result, the length of the crack increases, which in turn increases the stress and thus the crack propagation speed (31). This positive feedback continues until a critical stress is reached at which the main crack generates a side crack, which propagates perpendicular to the direction of the main crack (21). The formation of a side crack temporarily decreases the stress on the main crack. However, the stress increases again with the crack length as the main crack propagates further, until the stress becomes sufficient to generate another side crack. This repetitive process causes the main crack to produce N_b side cracks at quasiregular intervals l_b (21). These side cracks propagate as well and, because the stress between side cracks increases with decreasing distance between them (21, 31), are attracted to their nearest neighbor. For a 2D object, the resulting merger of side cracks produces $N_b/2$ fragments of typical size l_b (21). Yet another crack propagates from the merger of two side cracks, and the resulting $N_b/2$ side cracks of the next generation are also attracted to their nearest neighbor and form $N_b/4$ fragments of typical size $2l_b$ when they join. This process continues until no more side cracks remain, resulting in a scale-invariant PSD that, for a 3D spherical object, is approximately given by **1** (21, 29). Analogous processes produce scale invariance in a large variety of natural systems, including avalanches (30) and the fragmentation of rocks (29) and atomic nuclei (32).

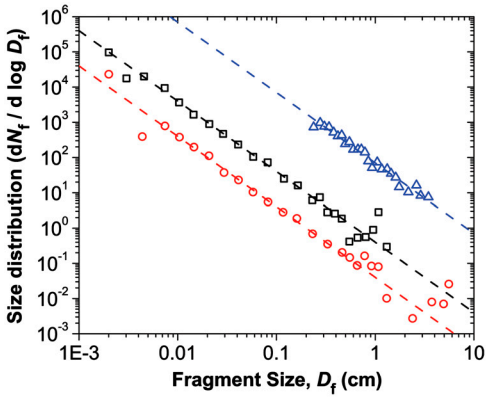

Fig. 1. Size distribution resulting from the fragmentation of a gypsum ball (blue triangles, taken from ref. 26) and two glass spheres (taken from ref. 28) of 2.4 cm (red circles) and 7.4 cm (black squares). The dashed lines denote the corresponding power laws with an exponent of −2 (see **1**).

The scale invariance produced by the merger of cracks can, however, hold only for an intermediate regime $x_0 < D_f < \lambda$, because the number of particles per infinitesimal bin diverges for $D_f \to 0$ and, similarly, the mass contained in each infinitesimal bin diverges for $D_f \to \infty$. Indeed, physically **1** cannot hold for very small particle sizes, because the "indivisible" constituents of the material (molecules, crystal cells, or individual dust particles in the case of dust aggregates—see below) have a finite length scale x_0 that prevents the creation of fragments of smaller sizes.

Whereas indivisible constituents prevent scale invariance at very small fragment sizes, the limited length λ to which side cracks propagate prevents scale variance at large fragment sizes (21, 29). Experiments show that, for fragile brittle materials in which the dissipation of the side crack propagation is not limiting the creation of fragments (29), the resulting large-size cutoff can be approximately described by the product of the power law (**1**) with an exponential function in terms of the fragment volume (26, 29):

$$\frac{dN_f}{d\ln D_f} \propto D_f^{-2} \exp\left[-\left(\frac{D_f}{\lambda}\right)^3\right], \qquad (D_f > x_0). \qquad [2]$$

Although the side crack propagation length λ is generally on the order of 10% of the size of the original object (26, 33), its exact value depends on the density of main cracks in the material. If a large number of main cracks are nucleated for a given sample size, then the side cracks cannot extend far before encountering another main crack and its side cracks, causing λ to be small. A larger input of energy nucleates more main cracks and therefore results in the large-size cutoff moving to smaller particle sizes (21, 27, 29).

Theoretical Model of Dust Emission

A brittle material is defined as "a material that is, more or less, linearly elastic up to a breaking strain where elasticity vanishes. […] At breaking the (local) material failure is complete, rapid, and (almost always) irreversible" (21). When stressed, dry soil aggregates usually fail as brittle materials (34–36). But, whereas the propagation of cracks in conventional brittle materials such as glass is dependent on material imperfections that locally weaken the material, the weakest points in dust aggregates are the surfaces of the constituent dust particle. As a consequence, the propagation of cracks in dust aggregates will proceed along the surfaces of the constituent dust particles.

When a saltating particle impacts a dust aggregate, the resulting PSD of fragments will fall into either the elastic, damage, or fragmentation regimes (defined above), depending on the impact energy and the dust aggregate cohesiveness (27). In order to predict the PSD of emitted dust aerosols, we therefore need to determine which regime is the dominant contributor to dust emission. Although the damage regime produces fragments, the fragmentation regime produces a much larger number of fragments per collision (27). Moreover, each impact in the damage regime nucleates cracks, thereby weakening the dust aggregate and increasing the likelihood that a subsequent impact will result in the fragmentation of the aggregate (31). For the above reasons, the present study assumes that, for most conditions, dust emission is predominantly due to fragmenting impacts. This assumption

is further justified by the occurrence of scale invariance in the emission of dust aerosols (see below), which is unique to the fragmentation regime (27).

Fragmentation of Dust Aggregates. Although the physics of dust aggregate fragmentation is expected to be similar to the fragmentation of conventional brittle materials such as glass, there is one important difference: the size of the indivisible constituents. In conventional brittle materials, these indivisible constituents are usually individual molecules or crystal units with sizes on the order of 10^{-10}–10^{-9} m, such that the small-size deviation from the power law of **1** due to the presence of indivisible constituents is only rarely observed (29). However, the indivisible constituents of dust aggregates are the discrete dust particles with much larger typical sizes of 10^{-7}–10^{-5} m (16, 17, 23). As a consequence, we expect the small-size deviation from the power law to occur at a typical fragment size of ~1 μm.

Many dust aerosols are aggregates themselves (17, 23, 37), such that an emitted dust aerosol consists of one or more soil particles of equal or smaller size. The production of dust aerosols with size D_d is thus proportional to the volume fraction of soil particles with size $D_s \leq D_d$ that contribute to the formation of these aerosols. That is, if the fraction of soil particles with size $D_s \leq D_d$ is doubled, then the production of aerosols with size D_d will be doubled as well, provided that the shape of the soil PSD remains constant. I therefore neglect any influence of changes in the shape of the soil PSD and assume that the production of aerosols of size D_d is proportional to the volume fraction of soil particles with size $D_s \leq D_d$,

$$\frac{dN_d}{d\ln D_d} \propto \int_0^{D_d} P_s(D_s)dD_s, \qquad [3]$$

where N_d is the normalized number of emitted dust aerosols with size D_d, and P_s is the fully dispersed PSD of PM20 soil particles. The distribution of fully disaggregated soil particles is usually described as a log-normal distribution (25):

$$P_s(D_s) = \frac{1}{\sqrt{2\pi}\ln(\sigma_s)}\exp\left\{-\frac{\ln^2(D_s/\tilde{D}_s)}{2\ln^2(\sigma_s)}\right\}, \qquad [4]$$

where σ_s is the geometric standard deviation, and $\tilde{D}_s$ is the median diameter by volume (2). The number and volume size distributions of emitted dust aerosols are then obtained by combining **2**–**4**,

$$\frac{dN_d}{d\ln D_d} = \frac{1}{c_N D_d^2}\left[1+\mathrm{erf}\left(\frac{\ln(D_d/\tilde{D}_s)}{\sqrt{2}\ln\sigma_s}\right)\right]\exp\left[-\left(\frac{D_d}{\lambda}\right)^3\right], \qquad [5]$$

$$\frac{dV_d}{d\ln D_d} = \frac{D_d}{c_V}\left[1+\mathrm{erf}\left(\frac{\ln(D_d/\tilde{D}_s)}{\sqrt{2}\ln\sigma_s}\right)\right]\exp\left[-\left(\frac{D_d}{\lambda}\right)^3\right], \qquad [6]$$

where V_d is the normalized volume of dust aerosols with size D_d, c_N and c_V are normalization constants, and erf is the error function (see p. 423 of ref. 2).

Note that Eqs. **5** and **6** are applicable only when dust emission is predominantly due to the fragmentation of soil aggregates. Eqs. **5** and **6** are, for example, not valid for (*i*) aerodynamically lifted dust (22), (*ii*) dust emitted mainly by impacts in the damage regime, which could occur for very cohesive soils, and (*iii*) dust with diameters larger than ~20 μm, which are more likely to occur as loose particles in the soil (17, 23), such that their emission is not always due to fragmenting impacts.

The Fully Dispersed PSD of Arid Soils. Eqs. **5** and **6** depend on the log-normal distribution parameters of fully dispersed soil particles with sizes extending from the submicron range up to 20 μm. Although measurements of soil PSDs extending into the submicron range have been published (38, 39), there are not nearly enough measurements to parameterize a spatially varying soil PSD in GCMs. To circumvent this problem, we must define a "typical" PM20 arid soil PSD.

Parameterizing a typical PM20 arid soil PSD is difficult, however, because there are few published arid soil PSDs that extend into the submicron range. A notable exception is the study of d'Almeida and Schütz (40), who reported such PSDs for six arid soils from across the Sahara (Table 1). These authors used wet sieving and optical and electron microscopy to determine the soil PSD from ~0.01–1,000 μm. Although the water in which d'Almeida and Schütz suspended their samples dispersed the soil to some degree, they did not fully disperse their samples, for example, by ultrasonic shaking or using a dispersing agent (38, 39). However, measurements suggest that the difference between the fully dispersed soil PSD and that obtained from suspension in water could be limited, especially in the clay size range (41).

I thus parameterize a typical PM20 arid soil PSD from the measurements of d'Almeida and Schütz (40), supplemented by laser diffraction measurements of actively eroding soils in Utah (42). A least-squares fitting technique was used to determine the most likely values of the log-normal parameters $\tilde{D}_s$ and σ_s for each individual soil (Table 1). The values of these parameters are surprisingly uniform, despite the wide range of soil textures and geographical locations represented. The average and standard deviation of the log-normal parameters of the eight soil PSDs are $\tilde{D}_s = 3.4 \pm 1.9$ μm and $\sigma_s = 3.0 \pm 0.4$, and the log-normal PSD with these average parameters appears to be a reasonable approximation to the eight available arid soil PSDs (see Fig. S1). However, the accuracy of the average values of $\tilde{D}_s$ and σ_s estimated in Table 1 remains uncertain because six of the eight soil PSDs are not fully dispersed (40) and because of the small number of soils represented.

Measurements of the Vertical Dust Flux. Testing the validity of Eqs. **5** and **6** requires measurements of the emitted dust PSD. Although measurements of the PSD of atmospheric dust aerosols are relatively abundant in the literature (37, 40, 43, 44), these measure-

Table 1. Values of the log-normal soil PSD parameters $\tilde{D}_s$ and σ_s

Study	Soil number	Soil texture	Geographical location	Best fit $\tilde{D}_s$, μm	Best fit σ_s
d'Almeida and Schütz (1983, ref. 40)	1	Loam	Mali	2.6	2.9
d'Almeida and Schütz (1983, ref. 40)	2	Silt	Senegal	1.6	3.4
d'Almeida and Schütz (1983, ref. 40)	3	Sand	Mali	1.7	2.8
d'Almeida and Schütz (1983, ref. 40)	4	Loamy sand	Algeria	7.2	3.7
d'Almeida and Schütz (1983, ref. 40)	5	Sand	Niger	2.1	2.9
d'Almeida and Schütz (1983, ref. 40)	6	Sandy loam	Sudan	4.9	2.7
Goldstein et al. (2005, ref. 42)	00-U36	Sand	Utah	3.0	2.8
Goldstein et al. (2005, ref. 42)	00-U37	Loam	Utah	3.8	2.8
Average and standard deviation				3.4 ± 1.9	3.0 ± 0.4

Values of $\tilde{D}_s$ and σ_s were obtained using least-squares fitting of Eq. **4** to the PSDs of eight arid soils with a range of textures and geographical origins (40, 42).

ments are not representative of the emitted dust PSD because they inherently include aerosol removal due to deposition. We instead require measurements of the size-resolved vertical dust flux produced by arid soils, which is a direct measure of the PSD of the emitted dust aerosols (45). A list of published size-resolved vertical dust flux measurements is given in Table S1.

To allow size-resolved vertical dust flux measurements from the six distinct soils investigated in the literature (14, 15, 45, 46) to be collectively compared against Eq. **5**, the measurements were processed as follows: Because measurements follow the power law of **1** in the range of 2–10 μm (see Fig. 2, *Inset*, and refs. 15 and 45), each set of measurements in that size range for a given soil and a given wind speed were fit to this power law. Measurements at all aerosol sizes for this given soil and wind speed were then normalized by the proportionality constant in the fitted power law to eliminate the strong dependence of the dust flux on the wind speed. For a given soil, this procedure put measurements at different wind speeds on an equal footing, except for the dependence of the shape of the dust PSD on the wind speed, which measurements suggest to be small (15, 44, 46). The normalized measurements at the various wind speeds for a given soil were then averaged for each particle size to reduce measurement noise and obtain the standard error. Because ref. 45 obtained only one reliable measurement per particle size, the standard error on these single measurements was estimated from the similar measurements of refs. 15 and 46.

Results

The theoretical emitted dust PSD (Eqs. **5** and **6**) depends on the parameters $\tilde{D}_s$, σ_s, and λ. The soil parameters $\tilde{D}_s = 3.4$ μm and $\sigma_s = 3.0$ are taken from Table 1, and the side crack propagation length $\lambda = 12 \pm 1$ μm is obtained from a least-squares fit to the measurements in Fig. 2. This latter result is in agreement both with the expected value of ∼10% (26, 33) of the typical dust aggregate size of ∼20–300 μm (17) and with the occurrence of scale invariance in dust emission up to a particle diameter of ∼10 μm (see Fig. 2, *Inset*, and discussion below). These values of $\tilde{D}_s$, σ_s, and λ yield $c_N = 0.9539$ μm and $c_V = 12.62$ μm for the normalization constants in Eqs. **5** and **6**.

Comparison of Theory with Measurements. Fig. 2 shows that the PSD of emitted dust aerosols is indeed scale invariant in the range of 2–10 μm, because it closely follows the predicted power law of **1**. Moreover, the PSD is reduced relative to the power law for small particle sizes (<2 μm), as predicted from the dust aggregate indivisible constituent size of ∼1 μm. The emitted dust PSD is also reduced relative to the power law for larger particle sizes (>10 μm), as predicted from the limited propagation length of side cracks. Measurements of the emitted dust PSD thus provide strong qualitative support for the dust emission theory presented above.

In addition to this qualitative agreement, Fig. 2 shows excellent quantitative agreement between theory and measurements. Do note that the theory is poorly constrained in the submicron range because of sparse measurements (14).

The final important result evident from Fig. 2 is the small amount of scatter between the dust flux datasets, even though these data were obtained for widely varying wind and soil conditions (Table S1). This similarity suggests that changes in the wind and soil conditions have only a limited effect on the emitted dust PSD, as also suggested by the insensitivity of dust aerosol PSDs to changes in wind speed and source region (37, 43, 44). Although more research is needed to fully verify this hypothesis, the apparent insensitivity of the emitted dust PSD to specific soil and wind conditions is highly fortuitous for regional and global dust modeling (44).

Comparison of Theory with Empirical Model Relations. Fig. 3 compares the theoretical expression of Eq. **6** to empirical relations used in regional models and GCMs. The theory is clearly an improvement over empirical model relations, because it provides much better agreement with measurements. In fact, both theory and measurements show that empirical model relations substantially overestimate the mass fraction of emitted clay aerosols ($D_d < 2$ μm), whereas they underestimate the fraction of emitted large silt aerosols ($D_d > \sim 5$ μm). The greater fraction of large silt aerosols found by measurements and predicted by theory is consistent with the underestimation of the long-range transport of large silt aerosols by GCMs (11, 12, 47).

With the exception of ref. 48, GCMs assume emitted clay mass fractions ranging from ∼10% (11, 12, 20, 49) to ∼35% (13, 18), whereas measurements and theory indicate an emitted clay fraction of $4.4 \pm 1.0\%$ for the average values and standard errors of $\tilde{D}_s$, σ_s, and λ listed above and in Table 1. Likewise, measured PSDs of dust aerosols indicate an atmospheric clay fraction of ∼10–20%, whereas GCMs predict an atmospheric clay fraction of ∼20–60% (Table S2). Further evidence that GCMs overestimate the emitted clay fraction was reported by Cakmur et al. (49), who found that optimal agreement of a GCM with measurements (e.g., dust aerosol optical depth, deposition, and PSD) requires a smaller clay fraction than normally used.

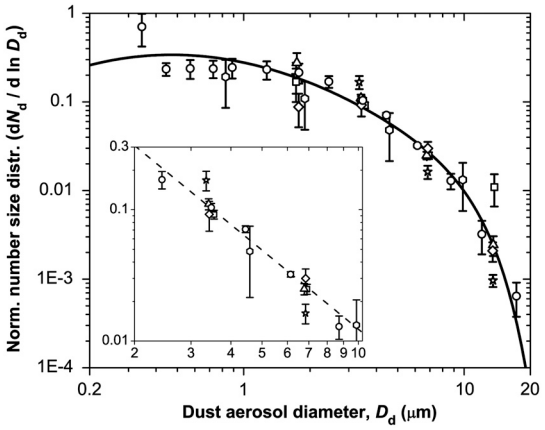

Fig. 2. Measurements with standard error of the normalized number size distribution of emitted dust aerosols [circles (14), squares (15), hexagons (45), triangles (soil 1 in ref. 46), stars (soil 2 in ref. 46), and diamonds (soil 3 in ref. 46)]. (*Inset*) Measurements in the size range of 2–10 μm only. The solid line denotes the theoretical prediction of Eq. **5**, and the dashed line denotes the power law of **1** observed for the fragmentation of brittle materials (see Fig. 1).

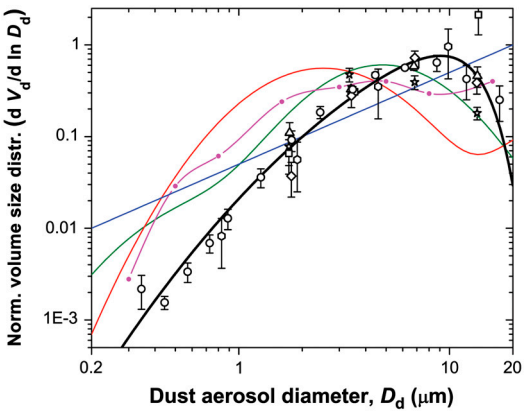

Fig. 3. The normalized volume size distribution of emitted dust aerosols used in 4 GCM studies [magenta line and circles (3), and blue (20), green (12), and red (13) lines]. The thick black line denotes the theoretical PSD of Eq. **6**, and symbols and error bars denote measurements as defined in Fig. 2.

Implications for Regional and Global Dust Modeling

Because the lifetime and radiative properties of clay and silt aerosols differ substantially, the overestimation of the clay fraction has implications for regional and global dust modeling. Whereas silt aerosols ($D_d > 2$ μm) have lifetimes up to a few days and can produce either a positive or negative forcing by absorbing and scattering both shortwave and longwave radiation, clay aerosols ($D_d < 2$ μm) have lifetimes on the order of a week and produce a strong negative radiative forcing by efficiently scattering shortwave radiation (3, 4, 18–20, 48). The overestimation of the clay fraction thus causes model errors in both the spatial distribution of dust and in the balance between dust radiative cooling and heating. On local and regional scales in dusty regions, this affects the magnitude of the dust radiative forcing and, depending on other factors such as the surface albedo and the height of the dust (4), can even change sign of the radiative forcing (50). These effects have implications for numerical weather forecasting as well as for regional climate predictions in dusty regions, especially if dust emissions change substantially in future climates, as hypothesized (7).

To investigate the effect of the clay fraction overestimation on simulations of the dust cycle on global scales, I obtain the mass-normalized radiative forcing for individual particle size bins from a recent GCM study (19) (see Fig. S2). [Note that refs. 18, 20, and 48 also report the radiative forcing of individual particle size bins, but these studies used dust optical properties that overestimate dust absorption of shortwave radiation according to recent insights (1, 13). Results from these studies are thus not used here.] The dust radiative forcings at the surface and at top of atmosphere (TOA) are then given by

$$F_{\text{surf}} = M_d \sum_i F^i_{\text{surf}} \int_{D^i_{\text{min}}}^{D^i_{\text{max}}} \frac{dV_d}{dD_d} dD_d;$$
$$F_{\text{TOA}} = M_d \sum_i F^i_{\text{TOA}} \int_{D^i_{\text{min}}}^{D^i_{\text{max}}} \frac{dV_d}{dD_d} dD_d, \quad [7]$$

where M_d is the global emission rate of dust aerosols, and i sums over the seven particle bins used in ref. 19, for which F^i_{surf} and F^i_{TOA} are the mass-normalized radiative forcings in $\text{W m}^{-2}\,\text{Tg}^{-1}$ Year at the surface and at TOA, and D^i_{min} and D^i_{max} are the bin's lower and upper size limits (Fig. S2).

The dust radiative forcing calculated with Eq. **7** is shown in Fig. 4 as a function of the global dust emission rate. For a given emission rate, the theoretical PSD of Eq. **6** predicts a surface radiative forcing that is a factor of ~2–6 less than predicted with empirical PSDs (3, 12, 13, 20), and also substantially smaller than predicted by GCM studies (13, 19, 51), with the exception of ref. 7. At TOA, the theoretical PSD produces a radiative forcing that is a factor of ~2–15 smaller than predicted with empirical PSDs and recent GCM studies (7, 13, 19, 51).

Fig. 4 thus indicates that the overestimation of the clay fraction causes GCMs either to underestimate the global dust emission rate or to overestimate the dust radiative cooling at the surface and especially at TOA. However, most GCM dust emission schemes are tuned to best match observations of the radiative characteristics of dust through comparisons against TOA radiative fluxes and dust aerosol optical depth (49, 52). Because these measurements are dominated by the long-lived and radiatively efficient clay fraction, correcting the overestimation of the clay fraction will likely increase the total mass of emitted dust aerosols at which GCMs produce optimal agreement with measurements (see Fig. S3 and figure 10 in ref. 49). It is thus more plausible that GCMs substantially underestimate the global dust emission rate than that GCMs substantially overestimate dust radiative forcing. This result implies that the deposition flux of dust to ocean ecosystems may be substantially larger than previously thought, especially close to source regions.

Note that possible cancellation of errors leaves open the possibility that GCMs do get both the global dust emission rate and the dust radiative forcing approximately correct. For example, if GCMs substantially overestimate the deposition of clay aerosols, then the overestimation of the emitted clay fraction could result in roughly correct concentrations of atmospheric clay aerosols, thereby producing reasonable predictions of the global dust emission rate and dust radiative forcing.

Dust aerosols also affect Earth's radiative budget by serving as cloud nuclei (5) and thereby modifying cloud properties, a process known as the "indirect effect" (1). A GCM with detailed cloud physics would be required to assess the effect of the revised dust size distribution on estimates of the dust indirect effect.

Summary and Conclusions

The present study indicates that dust emission is a scale-invariant process (Fig. 2, *Inset*) and uses this observation to derive a simple theoretical expression of the size distribution of emitted dust aerosols (Eqs. **5** and **6**). The theory is in excellent agreement with measurements (Fig. 2) and, when implemented in regional and global climate models, can resolve the substantial overestimation of the emitted clay fraction by these models (Fig. 3).

On local and regional scales, the overestimation of the emitted clay fraction by models has likely caused errors in the magnitude and, depending on local variables such as the suface albedo (4), potentially the sign of the modeled dust radiative forcing (50), which has implications for numerical weather forecasting and regional climate predictions in dusty regions. On a global scale, the overestimation of the emitted clay fraction has likely caused GCMs to underestimate the size of the global dust cycle (Fig. 4 and Fig. S3). This latter result implies that the deposition flux of dust to oceans, and the resulting effect on atmospheric green-

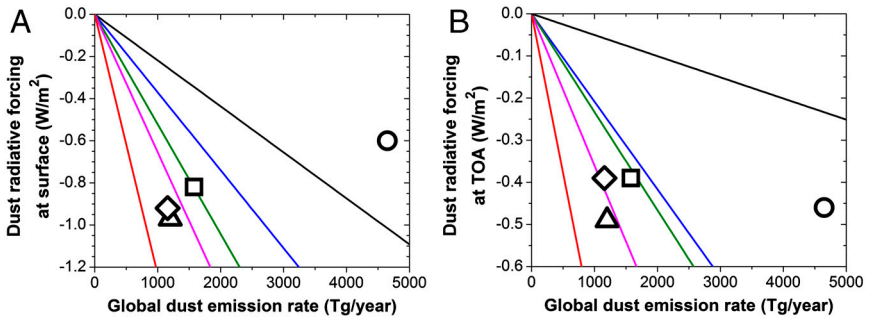

Fig. 4. The dust radiative forcing at the surface (*A*) and at TOA (*B*) calculated from Eq. **7** with the theoretical PSD (Eq. **6**, solid black line) and with four empirical PSDs used in GCMs and plotted in Fig. 3 [magenta (3), blue (20), green (12), and red (13) lines]. Included are radiative forcings calculated by four recent GCM studies [squares (19), circles (7), triangles (51), and diamonds (13)] that used dust shortwave absorption properties consistent with recent findings (1, 13).

house gas concentrations through the fertilization of marine biota (6), may be substantially larger than previously thought, especially close to dust source regions.

The theoretical model presented here could be applied to fragmentation in analogous physical systems where the creation of small fragments is limited by the presence of indivisible particles. This includes dust emission on Mars and the fragmentation of small asteroids (53), granular rocks (29), and other brittle materials with a granular or crystal structure.

ACKNOWLEDGMENTS. I thank Annick Pouquet for pointing out the relevance of the scale-invariance literature to dust emission, Stephanie Woodward and Yves Balkanski for providing me with the dust emission rates of the Woodward (48) and Balkanski et al. (13) studies, and Ted Zobeck, Marco Bittelli, Inez Fung, Natalie Mahowald, Charlie Zender, and an anonymous reviewer for many excellent suggestions. Comments by Shanna Shaked, John Seinfeld, Alexandra Jahn, Julie Theriault, Malcolm Brooks, Annick Pouquet, Charlie Zender, and Natalie Mahowald improved the clarity of the manuscript. The National Center for Atmospheric Research is sponsored by the National Science Foundation.

1. Forster P, et al. (2007) Changes in atmospheric constituents and in radiative forcing. *Climate Change 2007: The Physical Science Basis*, eds S Solomon et al. (Cambridge Univ Press, Cambridge, UK).
2. Seinfeld JH, Pandis SN (1998) *Atmospheric Chemistry and Physics: From Air Pollution to Climate Change* (Wiley, New York).
3. Tegen I, Lacis AA (1996) Modeling of particle size distribution and its influence on the radiative properties of mineral dust aerosol. *J Geophys Res* 101:19237–19244.
4. Liao H, Seinfeld JH (1998) Radiative forcing by mineral dust aerosols: Sensitivity to key variables. *J Geophys Res* 103:31637–31645.
5. DeMott PJ, et al. (2010) Predicting global atmospheric ice nuclei distributions and their impacts on climate. *Proc Natl Acad Sci USA* 107:11217–11222.
6. Jickells TD, et al. (2005) Global iron connections between desert dust, ocean biogeochemistry, and climate. *Science* 308:67–71.
7. Mahowald NM, et al. (2006) Climate response and radiative forcing from mineral aerosols during the last glacial maximum, pre-industrial, current and doubled-carbon dioxide climates. *Geophys Res Lett* 33:L20705.
8. Jansen E, et al. (2007) Palaeoclimate. *Climate Change 2007: The Physical Science Basis. Contribution of Working Group I to the Fourth Assessment Report of the Intergovernmental Panel on Climate Change*, eds S Solomon et al. (Cambridge Univ Press, Cambridge, UK).
9. Prospero JM (1999) Assessing the impact of advected African dust on air quality and health in the eastern United States. *Hum Ecol Risk Assess* 5:471–479.
10. Evan AT, et al. (2006) New evidence for a relationship between Atlantic tropical cyclone activity and African dust outbreaks. *Geophys Res Lett* 33:L19813.
11. Ginoux P, et al. (2001) Sources and distributions of dust aerosols simulated with the GOCART model. *J Geophys Res* 106:20255–20273.
12. Zender CS, Bian HS, Newman D (2003) Mineral Dust Entrainment and Deposition (DEAD) model: Description and 1990s dust climatology. *J Geophys Res* 108:4416.
13. Balkanski Y, Schulz M, Claquin T, Guibert S (2007) Reevaluation of mineral aerosol radiative forcings suggests a better agreement with satellite and AERONET data. *Atmos Chem Phys* 7:81–95.
14. Sow M, Alfaro SC, Rajot JL, Marticorena B (2009) Size resolved dust emission fluxes measured in Niger during 3 dust storms of the AMMA experiment. *Atmos Chem Phys* 9:3881–3891.
15. Gillette DA, Blifford IH (1974) Influence of wind velocity on size distributions of aerosols generated by wind erosion of soils. *J Geophys Res* 79:4068–4075.
16. Alfaro SC, Gomes L (2001) Modeling mineral aerosol production by wind erosion: Emission intensities and aerosol size distributions in source areas. *J Geophys Res* 106:18075–18084.
17. Shao Y (2001) A model for mineral dust emission. *J Geophys Res* 106:20239–20254.
18. Miller RL, Tegen I, Perlwitz J (2004) Surface radiative forcing by soil dust aerosols and the hydrologic cycle. *J Geophys Res* 109:D04203.
19. Miller RL, et al. (2006) Mineral dust aerosols in the NASA Goddard Institute for Space Sciences ModelE atmospheric general circulation model. *J Geophys Res* 111:D06208.
20. Yue X, Wang HJ, Liao H, Fan K (2010) Simulation of dust aerosol radiative feedback using the GMOD: 2. Dust-climate interactions. *J Geophys Res* 115:D04201.
21. Astrom JA (2006) Statistical models of brittle fragmentation. *Adv Phys* 55:247–278.
22. Shao YP (2008) *Physics and Modelling of Wind Erosion* (Springer, Heidelberg), 2nd Ed.
23. Alfaro SC, Gaudichet A, Gomes L, Maille M (1997) Modeling the size distribution of a soil aerosol produced by sandblasting. *J Geophys Res* 102:11239–11249.
24. Kok JF, Renno NO (2009) A comprehensive numerical model of steady state saltation (COMSALT). *J Geophys Res* 114:D17204.
25. Kolmogorov AN (1941) On the logarithmically normal distribution law of particle sizes under grinding. *Dokl Akad Nauk SSSR* 31:99–101.
26. Oddershede L, Dimon P, Bohr J (1993) Self-organized criticality in fragmenting. *Phys Rev Lett* 71:3107–3110.
27. Kun F, Herrmann HJ (1999) Transition from damage to fragmentation in collision of solids. *Phys Rev E* 59:2623–2632.
28. Gilvarry JJ, Bergstrom BH (1961) Fracture of brittle solids. 2. Distribution function for fragment size in single fracture (experimental). *J Appl Phys* 32:400–410.
29. Astrom JA, Ouchterlony F, Linna RP, Timonen J (2004) Universal dynamic fragmentation in D dimensions. *Phys Rev Lett* 92:245506.
30. Bak P, Tang C, Wiesenfeld K (1987) Self-organized criticality—an explanation of 1/*F* noise. *Phys Rev Lett* 59:381–384.
31. Herrmann HJ (1990) Introduction to basic notions and facts. *Statistical Models for the Fracture of Disordered Media*, eds HJ Herrmann and S Roux (Elsevier, Amsterdam).
32. Bondorf JP, Botvina AS, Iljinov AS, Mishustin IN, Sneppen K (1995) Statistical multifragmentation of nuclei. *Phys Rep* 257:133–221.
33. Redner S (1990) Fragmentation. *Statistical Models for the Fracture of Disordered Media*, eds HJ Herrmann and S Roux (Elsevier, Amsterdam).
34. Lee IK, Ingles OG (1968) Soil mechanics selected topics. *The Brittle Failure of Unsaturated Soils, Stabilized Soils, and Rocks*, ed IK Lee (Elsevier, New York), pp 251–294.
35. Braunack MV, Hewitt JS, Dexter AR (1979) Brittle-fracture of soil aggregates and the compaction of aggregate beds. *J Soil Sci* 30:653–667.
36. Perfect E, Kay BD (1995) Brittle-fracture of fractal cubic aggregates. *Soil Sci Soc Am J* 59:969–974.
37. Reid JS, et al. (2003) Comparison of size and morphological measurements of coarse mode dust particles from Africa. *J Geophys Res* 108:8593.
38. Bittelli M, Campbell GS, Flury M (1999) Characterization of particle-size distribution in soils with a fragmentation model. *Soil Sci Soc Am J* 63:782–788.
39. Zobeck TM (2004) Rapid soil particle size analyses using laser diffraction. *Appl Eng Agric* 20:633–639.
40. d'Almeida GA, Schütz L (1983) Number, mass and volume distributions of mineral aerosol and soils of the Sahara. *J Clim Appl Meteorol* 22:233–243.
41. Buurman P, Pape T, Muggler CC (1997) Laser grain-size determination in soil genetic studies. 1. Practical problems. *Soil Sci* 162:211–218.
42. Goldstein H, et al. (2005) Particle-size, $CaCO_3$, chemical, magnetic, and age data from surficial deposits in and around Canyonlands National Park, Utah. US Geological Survey.
43. Maring H, Savoie DL, Izaguirre MA, Custals L, Reid JS (2003) Mineral dust aerosol size distribution change during atmospheric transport. *J Geophys Res* 108:8592.
44. Reid JS, et al. (2008) Dynamics of southwest Asian dust particle size characteristics with implications for global dust research. *J Geophys Res* 113:D14212.
45. Gillette DA, Blifford IH, Fenster CR (1972) Measurements of aerosol size distributions and vertical fluxes of aerosols on land subject to wind erosion. *J Appl Meteor* 11:977–987.
46. Gillette DA (1974) On the production of soil wind erosion having the potential for long range transport. *J Rech Atmos* 8:734–744.
47. Grini A, Zender CS (2004) Roles of saltation, sandblasting, and wind speed variability on mineral dust aerosol size distribution during the Puerto Rican Dust Experiment (PRIDE). *J Geophys Res* 109:D07202.
48. Woodward S (2001) Modeling the atmospheric life cycle and radiative impact of mineral dust in the Hadley Centre climate model. *J Geophys Res* 106:18155–18166.
49. Cakmur RV, et al. (2006) Constraining the magnitude of the global dust cycle by minimizing the difference between a model and observations. *J Geophys Res* 111:D06207.
50. Patadia F, Yang ES, Christopher SA (2009) Does dust change the clear sky top of atmosphere shortwave flux over high surface reflectance regions? *Geophys Res Lett* 36: L15825.
51. Shell KM, Somerville RCJ (2007) Direct radiative effect of mineral dust and volcanic aerosols in a simple aerosol climate model. *J Geophys Res* 112:D03205.
52. Woodage MJ, Slingo A, Woodward S, Comer RE (2010) UK HiGEM: Simulations of desert dust and biomass burning aerosols with a high-resolution atmospheric GCM. *J Climate* 23:1636–1659.
53. Richardson DC, Leinhardt ZM, Melosh HJ, Bottke WF, Asphaug E (2002) Gravitational aggregates: Evidence and evolution. *Asteroids III*, eds WF Bottke, A Cellino, P Paolicchi, and R Binzel (Univ Arizona Press, Tucson), pp 501–515.